Wang, L., Hainzl, S., Mai, P. M. (2017): To which level did the 2010 M 8.8 Maule earthquake fill the pre-existing seismic gap? - *Geophysical Journal International*, *211*, 1, pp. 498—511.

DOI: http://doi.org/10.1093/gji/ggx304

Geophysical Journal International

Geophys. J. Int. (2017) **211,** 498–511
Advance Access publication 2017 August 3
GJI Seismology

doi: 10.1093/gji/ggx304

To which level did the 2010 M 8.8 Maule earthquake fill the pre-existing seismic gap?

Lifeng Wang,[1] Sebastian Hainzl[2] and P. Martin Mai[3]

[1]*State Key Laboratory of Earthquake Dynamics, Institute of Geology, China Earthquake Administration, Beijing* 100029*, China. E-mail: wanglf@ies.ac.cn; chsxwlf@hotmail.com*
[2]*Deutsches GeoForschungsZentrum GFZ, Potsdam D-*14473*, Germany*
[3]*King Abdullah University of Science and Technology (KAUST), Thuwal* 23955*, Saudi Arabia*

Accepted 2017 July 19. Received 2017 July 16; in original form 2016 November 30

SUMMARY

There is a long-standing debate whether or not the 2010 M 8.8 Maule earthquake filled a pre-existing seismic gap in which no large earthquake occurred for about 200 yr. Utilizing the inversion approach of Wang *et al*. that considers elastic strain accumulation and strain release during the earthquake cycle and includes the fault-coupling state as prior information in coseismic slip modelling, we investigate the inter- and coseismic slip balance for the 2010 M 8.8 Maule earthquake. The coseismic slip model is obtained as the product of three components: the interseismic backslip rate, the strain accumulation time, and the fraction of coseismically released slip potency (the product of slip and slip area) that may either fully or partially release the local strain. We construct slip models using the Slab1.0 fault geometry, and constrain the strain accumulation time for the 2010 Maule earthquake based on historical large earthquakes in the region. The results demonstrate that two slip clusters (north and south of the hypocentre) are required to model the geodetically measured coseismic displacements. The slip patch south of the hypocentre is located in a strongly coupled zone, and possibly released the local strain completely. The slip area north of the hypocentre overlaps with the interseismically creeping zone in which strain buildup may be low. The northern slip patch released higher slip potency than accumulated since the last mega-event in 1751, suggesting a possible dynamic overshoot during coseismic rupture (under the assumption that the last major earthquake has reset the regional strain). Alternatively, the last big event may not have fully released the strain in this region. Our study reveals that the Maule earthquake, combing its coseismic and post-seismic slip over 1.3 yr, released ∼67–72 per cent of the local strain. Remaining strain is concentrated mainly south of the hypocentre, with potency equivalent to an M 8.4 event considering strain accumulation for 259 yr (since 1751).

Key words: Seismicity and tectonics; Subduction zone processes.

1 INTRODUCTION

The seismic coupling of a fault zone is an important factor controlling its seismic activity, particularly in subduction zones (e.g. Ruff & Kanamori 1980; Peterson & Seno 1984; Pacheco *et al.* 1993; Scholz & Small 1997). For example, earthquakes in strongly coupled zones (e.g. Chile or Alaska) are much larger than those in the weakly coupled zones (e.g. Marianas). Therefore, investigating and quantifying the seismic coupling behaviour during the interseismic phase may provide information regarding possible future strong earthquakes, and thus may be important for regional seismic hazard assessment. Owing to the rapid development and increased availability of geodetic measurements in the last decades (e.g. Global Positioning System, GPS, and Interferometric Synthetic Aperture Radar, InSAR), data of dense ground-surface displacements (and displacement rates) allow investigations of the (inter-) seismic coupling states and coseismic rupture processes.

In this study, we examine the 2010 M 8.8 Maule (Chile) subduction-zone earthquake that occurred within a seismic gap (located between 35°S and 37°S), as inferred from both seismic and GPS data (McCann *et al.* 1979; Campos *et al.* 2002; Ruegg *et al.* 2002; Moreno *et al.* 2008; Ruegg *et al.* 2009). This region has not experienced significant earthquakes ($M > 8$) for nearly 200 yr. Several studies examined the interseismic coupling in this region by inverting displacement rates measured before the Maule earthquake (Moreno *et al.* 2008; Ruegg *et al.* 2009; Metois *et al.* 2012).

Generally, the spatial correlation between the coupling zone and the rupture areas of large earthquakes is thought to reflect the process of regional strain accumulation and release. However, due to the non-uniqueness of fault slip inversions (e.g. Mai *et al.* 2016), controversial results have been reported for the 2010 Maule earthquake. Moreno *et al*. (2010) stated that the interseismic coupling/locking zone is closely correlated with the main coseismic rupture of the Maule earthquake, suggesting that this earthquake has filled the seismic gap and that most of the interseismically accumulated strain has been released. In contrast, other studies (Lorito *et al.* 2011; Moreno *et al.* 2012) reported that the seismic gap was only partially filled by the 2010 Maule earthquake, leaving a strongly coupled zone unbroken. This suggests a high potential that large earthquakes again occur in this region in the near future.

These ambiguous conclusions are born out of different slip (and backslip/coupling) models, which are a consequence of the non-uniqueness of fault slip inversions (Mai & Thingbaijam 2014; Mai *et al.* 2016) due to limited surface observations, different fault parameterizations (e.g. Page *et al.* 2009), alternative inversion algorithms (e.g. Du *et al.* 1992), different assumptions on measurement uncertainties (e.g. Lohman & Simons 2005), as well as divergent simplifications of Earth models. In addition, the chosen smoothing constraints applied in traditional least-squares (LS) inversions affect the final solution, and possibly subsequent interpretations as well. For the Maule study case, the ambiguity also stems from inconsistent modelling strategies for the inter- and coseismic phase. For example, a coseismic slip model was constructed in an elastic half-space (Lorito *et al.* 2011) or determined assuming a planar fault (Moreno *et al.* 2010), but was then compared with the interseismic coupling derived from a 3-D viscoelastic model. Furthermore, previous investigations on the spatial correlation between interseismic coupling and coseismic rupture were based on visual comparisons, and therefore lack quantitative evaluation.

In this study, we self-consistently integrate inter- and coseismic displacements, considering strain accumulation (during the interseismic phase) and strain release (during earthquake rupture), into coseismic slip modelling based on the elastic rebound theory (Reid 1910), which conveys earthquakes occur as the result of strain built up over a long time period. We assume that interseismic coupling does not change with time during the interseismic phase, as suggested by displacement time series measured in the last decades in the well-instrumented regions (e.g. Gomez *et al.* 2007). Depending on constant or time-varying fault strength and earthquake stress drops, earthquakes occur periodically, randomly or clustered. Studies on the seismicity of East Pacific Rise Transform fault (McGuire 2008) and palaeoearthquakes (e.g. Sykes & Menke 2006) have indicated that earthquakes happen in a quasi-periodic manner, instead of a Poisson-type sequence, implying earthquake predictability to some degree (Jordan 2006).

A seismic gap refers to a fault zone that has not experienced a large earthquake for a significant period of time, and is expected to release higher seismic moment than other regions of this fault. The seismic activity within the seismic gap is relatively low (McCann *et al.* 1979), and hence we ignore stress perturbations of possible small earthquakes within the seismic gap during the interseismic phase. We consider the coseismic phase as a step function, as seen in the long-term continuous GPS measurements, and ignore the complex dynamic rupture process.

We calculate the slip balance between inter- and coseismic phases based on the inversion approach of Wang *et al*. (2015) to obtain a first-order understanding of the strain accumulation and release process within the seismic gap in which the 2010 M 8.8 Maule earthquake occurred. With the constructed first-order model of slip balance, we then discuss the impact of post-seismic relaxation processes of the large earthquakes.

In the following, we first briefly summarize the inversion method for coseismic slip using interseismic coupling as prior information (details in Wang *et al*. 2015). We then present the model setup and data (Section 3), and the modelling results for the 2010 Maule earthquake (Section 4). In Section 5, we discuss previously published inter- and coseismic slip models, and the seismic potency release of the Maule earthquake with respect to the regional interseismic strain accumulation. Our results indicate a possible slip-overshoot effect during coseismic rupture north of the hypocentre, while the left-over strain energy for a ∼M 8.4 earthquake may still be stored south of the hypocentre.

2 METHODOLOGY

To quantify the slip balance between the inter- and coseismic phase, we conduct coseismic slip inversion using interseismic coupling as prior information (Wang *et al.* 2015). This method assumes a linear correlation between the coseismic slip ($\mathbf{m}_{l\times1}$, with l being the number of discretized fault patches) and the interseismic coupling state. The latter is modelled using the backslip rate ($\mathbf{r}_{l\times1}$) based on the geodetically measured long-term interseismic surface displacement rates (Savage 1983) via $\mathbf{m} = T_\mathrm{r}\mathbf{R}_{l\times l}\boldsymbol{\kappa}$, where $\mathbf{R}_{l\times l}$ is the diagonal matrix of $\mathbf{r}$, T_r represents the strain accumulation time until the main shock, and $\boldsymbol{\kappa}_{l\times1} \in [\mathbf{0}, \mathbf{1}]$ quantifies the spatially variable potency release of the coseismic rupture. $[\boldsymbol{\kappa}]_i = 1$ ($i = 1 \ldots l$) denotes 100 per cent release of the interseismically accumulated slip potency (the product of slip and slip area, Perfettini *et al.* 2010) on the ith fault patch (conversely, $[\boldsymbol{\kappa}]_i = 0$ indicates no coseismic slip at location i). Let $\mathbf{K} = T_\mathrm{r}\boldsymbol{\kappa}$, then the following linear equation applies

$$\begin{vmatrix} \mathbf{GR} \\ \lambda^2\mathbf{LR} \\ \gamma^2\mathbf{I} \end{vmatrix} \mathbf{K} = \begin{vmatrix} \mathbf{d} \\ \mathbf{0} \\ \mathbf{0} \end{vmatrix}, \tag{1}$$

where $\mathbf{d}_{n\times1}$ are n measurements of coseismic displacements, and $\mathbf{G}_{n\times l}$ is the matrix of Green's function for a chosen fault geometry. $\mathbf{L}_{l\times l}$ and $\mathbf{I}_{l\times l}$ denote the discrete Laplacian operator (Herrmann 1976; Jónsson *et al.* 2002) and the identity matrix, respectively, and are applied as a smoothing condition to coseismic slip and minimizing constraint to $\mathbf{K}$. λ^2 and γ^2 are the corresponding hyperparameters.

The strain accumulation time T_r until the main shock, if available from a catalogue of historical earthquakes can be adopted to constrain $\mathbf{K}$, so that $[\mathbf{K}]_i \leq T_\mathrm{r}$ ($\mathbf{K} = T_\mathrm{r}\boldsymbol{\kappa}$ with $\boldsymbol{\kappa} \in [\mathbf{0}, \mathbf{1}]$), such that the potency release of the main shock is restricted to be not larger than that stored in the preceding interseismic period T_r. With this constraint, we evaluate the remaining strain after the main shock to gain a first-order understanding of the strain accumulation and release process. Secondary complexity of the faulting dynamics, such as dynamic overshoot may then be subsequently analysed by modelling the displacement residuals.

It is noteworthy that eq. (1) has a slightly modified form of the traditional fault slip inversion with smoothing constraints

$$\begin{vmatrix} \mathbf{G} \\ \lambda^2\mathbf{L} \end{vmatrix} \mathbf{m} = \begin{vmatrix} \mathbf{d} \\ \mathbf{0} \end{vmatrix}. \tag{2}$$

We perform the inversion using an LS approach. First, the hyperparameters λ^2 and γ^2 are determined based on cross-validation (Wang *et al*. 2015), and then we solve for the unknown $\mathbf{m}$ for the

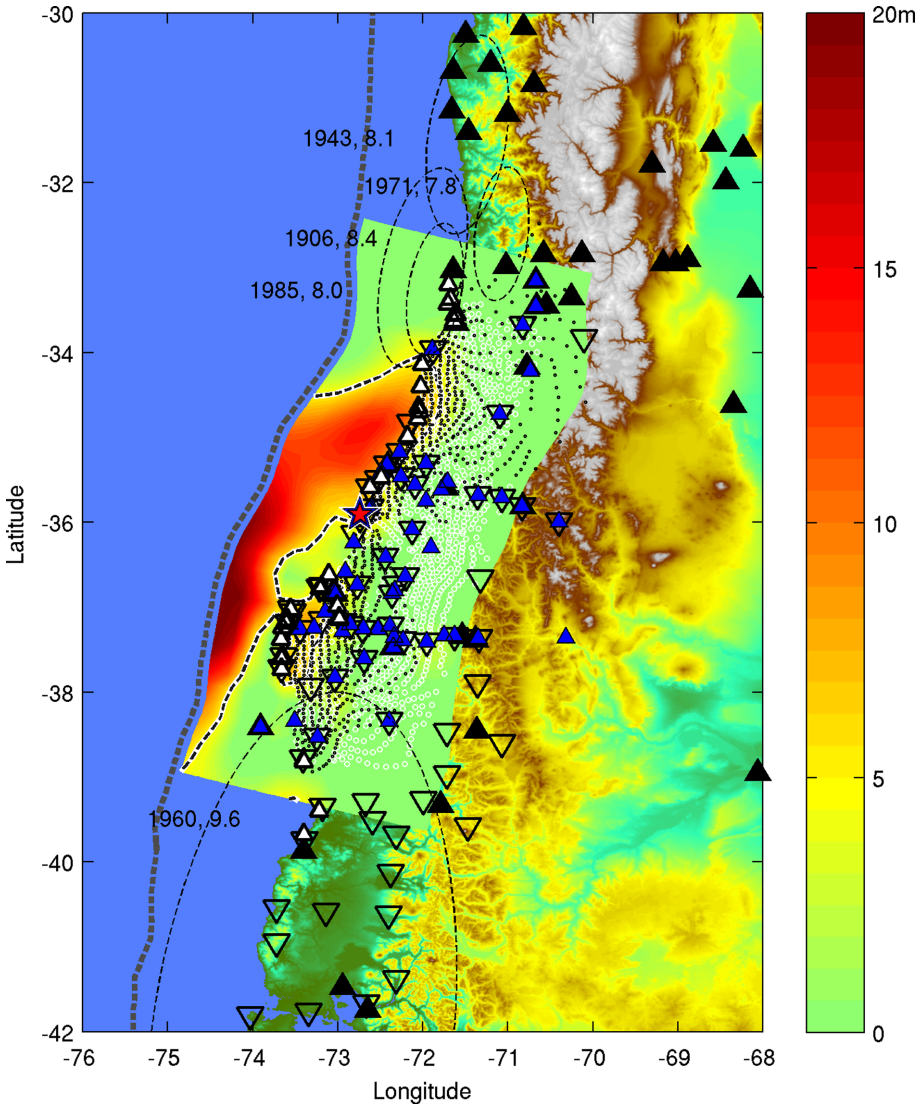

Figure 1. Study region and observation networks: GPS sites with interseismic measurements (blue triangles); GPS sites with the coseismic displacement measurements (black-filled triangles for continuous GPS and downward-open triangles for campaign GPS); ascending/descending InSAR measurements (black dots/white circles) and land-level changes (white-filled triangles). The ellipses mark the neighbouring significant earthquakes since 1900 from ISC GEM catalogue (Storchak *et al.* 2013). Ellipses (eccentricity ∼0.9) are centred at the hypocentres of the large historical earthquakes with areas calculated from the earthquake magnitudes by empirical relations (Wells & Coppersmith 1994). The coseismic slip inverted for the 2010 M 8.8 Maule earthquake is colour-coded, the red star marks its hypocentre. The dashed curve marks the trench.

model without the interseismic constraint (or **K** for the model with the interseismic constraint) and its uncertainties using the obtained hyperparameters (details in Supporting Information Section S2 and Wang *et al.* 2015). For the model constrained by interseismic coupling, the coseismic slip is calculated by $\mathbf{m} = \mathbf{Kr}$, after **K** is inverted. The potency release level ($\boldsymbol{\kappa}$) is calculated from $\mathbf{K}/T_{\mathrm{r}}$. In this study, T_{r} (correspondingly the maximum **K**) is determined according to the historical earthquake records in this region.

3 DATA AND FAULT MODEL

In this study, we use the interseismic GPS data compiled from several geodetic studies (Klotz *et al.* 2001; Ruegg *et al.* 2002; Moreno *et al.* 2008; Ruegg *et al.* 2009) and the published coseismic GPS displacements (Tong *et al.* 2010; Vigny *et al.* 2011; Moreno *et al.* 2012; Lin *et al.* 2013), all of which were processed in the fixed South America reference frame. Published InSAR data for the Maule earthquake are available from Tong *et al.* (2010). We also use the published land-level change data (Melnick *et al.* 2012). All measurement sites are shown in Fig. 1. The dense interseismic and coseismic displacement measurements enable us to quantitatively evaluate the interseismic strain accumulation and coseismic strain release in this region.

We construct the fault geometry using Slab 1.0, a 3-D model for subduction zones built from historic earthquake catalogues, CMT solutions, active seismic profiles, global plate boundaries, bathymetry and sediment thickness information (Hayes *et al.* 2012). For consistency, we model fault slip for both inter- and coseismic phase using this fault geometry. The area for the coseismic slip inversion has a dimension of ∼800 × 400 km^2, and reaches a depth

of 110 km. To match the irregular shape of the subduction zone, the fault plane is meshed by triangles with dimension of $\sim 13 \times 13$ km^2. For the inversion for interseismic backslip, we consider a larger area centred on the coseismic rupture (dimension $\sim 1200 \times 600$ km^2). This zone is much larger than the spatial extent of the interseismic measurements on the surface, and chosen as such because the interseismic coupling is not as localized as the coseismic rupture, but more widely distributed along the subduction zone. An interseismic coupling model based on the fault plane, comparable to or smaller than the observation network, may result in strong coupling over the entire chosen fault plane, if the measurements include also signals of coupling outside of the applied small fault. Although we model coupling for a large fault plane that extends below the Moho, the modelled deep coupling may not be entirely realistic due to predominantly viscoelastic behaviour at such depths that are unfavourable for elastic strain accumulation (Wang *et al.* 2012a). Furthermore, the observation network has little resolution at these depths and in the bounding region of the adopted large fault. Nevertheless, the coseismic slip zone of the 2010 Maule event is well covered by interseismic observation and is well constrained as indicated by the checkerboard test (see Supporting Information Fig. S2).

To investigate the coupling correlation between the inter- and coseismic phases, we use a fixed rake angle of 112°, which is the dominant rake angle for the coseismic rupture of the Maule earthquake (Vigny *et al.* 2011; Moreno *et al.* 2012, see also Supporting Information Fig. S1); this rake-angle is also consistent with the orientation of plate convergence. The interseismic backslip rate is assumed to be along the same direction, but in the sense of normal faulting, opposite to the direction of coseismic slip.

Across-fault material contrast are well understood in subduction zones, and may influence dynamic rupture process of earthquakes (e.g. Brietzke *et al.* 2009). For static slip modelling, the coseismic stress drop in the bi-material host rock produces asymmetric surface displacements at opposite sides of the fault (e.g. Wang *et al.* 2012b). However, observing such asymmetry is very difficult for ocean-continent subduction zones because surface displacements are measured only on the continental side. Therefore, we simply construct the matrix of Green's function using an elastic half-space (Okada 1985; Meade 2007). We have also tested a layered model, and found that the predicted coseismic displacements are similar as those based on the elastic half-space; therefore, we focus on the results for an elastic half-space. Deep viscoelastic relaxation is important during post-seismic phase and its impact will be discussed (in Section 5.4) to further improve our understanding of slip balance in the seismic cycle.

Based on our model setup, we conduct checkerboard tests to evaluate the resolving capability of our inversion with the available observational networks. The optimal solution and its uncertainties are determined from the marginal probability densities (marginal PDFs, see Supporting Information Figs S2d and e) constructed from 1000 modelling results that account for measurement errors. Other model errors, such as fault geometry and complex material property, will be discussed in Section 5, and are ignored here for simplicity. Specifically, we carry out 1000 slip inversions based on normally distributed random realizations of 1000 datasets, simulated using the mean values of surface displacements and the corresponding standard deviation of measurement errors. For more details, we refer to the Supporting Information (Section S2). The results given in the Supporting Information (Figs S2–S6) indicate that the interseismic observational network lacks resolution in the bounding regions, but generally has good resolution in the coseismic rupture zone of the 2010 Maule earthquake (marked by dashed curve in Supporting Information Figs S2a and b). The continuous GPS sites for coseismic displacement measurements poorly resolve the near-trench region, but generally resolve the slip with minimal patch size of $\sim 80 \times 80$ km in the fault centre (Supporting Information Fig. S4). Additional campaign GPS, InSAR and land-level change data help to improve the resolution for coseismic slip modelling, and generally well resolve the entire fault plane (Supporting Information Figs S5 and S6).

4 RESULTS

We now present our slip-inversion results. We first use our model setup to construct inter- and coseismic slip models separately, without considering their correlation. A simple visual comparison between the inter- and coseismic slip model may provide insights into the strain accumulation and release (e.g. Lorito *et al.* 2011; Moreno *et al.* 2012). We then model the coseismic slip, constrained by interseismic coupling, to quantitatively evaluate the potency release level of the 2010 Maule earthquake.

4.1 Slip models without consideration of inter- and coseismic correlation

4.1.1 Interseismic backslip

Interseismic coupling models for this region have been presented previously (Moreno *et al.* 2008; Ruegg *et al.* 2009; Metois *et al.* 2012). In this study, we invert for interseismic backslip based on the model setup described above and eq. (2). We constrain the interseismic backslip rate to be no larger than the convergence rate of 6.8 cm yr^{-1} between the Nazca and the South America plate (Vigny *et al.* 2011). A high backslip rate suggests strong interseismic coupling.

During the inversion, the hyperparameter λ^2 is determined using cross-validation (Supporting Information Fig. S7). The resulting optimal backslip model and its uncertainties are shown in Fig. 2. The uncertainties are determined from the marginal PDFs based on 1000 modelling results, similar to the checkerboard test shown in Supporting Information Fig. S2. The backslip model well explains the interseismic displacement rates with high Variance Reduction (VR) of >95 per cent, where $VR = (1 - \frac{\Delta\mathbf{x}\Sigma^{-1}\Delta\mathbf{x}}{\mathbf{x}^{\mathrm{T}}\Sigma^{-1}\mathbf{x}}) \times 100$ per cent, with $\Delta\mathbf{x} = \mathbf{x} - \hat{\mathbf{x}}$, the difference between the observations ($\mathbf{x}$) and the modelling results ($\hat{\mathbf{x}}$), and Σ^{-1} being the covariance matrix of $\mathbf{x}$. The modelled surface displacements are provided in Supporting Information Fig. S7b. The interseismic backslip model (Fig. 2a) indicates an elongated region of strong coupling that extends across the hypocentral area (marked by star in Fig. 2). The modelling uncertainties (Fig. 2b) suggest that in regions of major coseismic slip (e.g. Figs 1 and 3a and Supporting Information Fig. S2a) the uncertainties are small.

We have applied a fault plane much larger than the coverage of the interseismic observation network to avoid the signal outside the seismogenic zone (such as inelastic deformation below the Moho depth) being mistakenly interpreted as seismic coupling. However, as mentioned in Section 3, the modelled deep backslip is likely unrealistic, as also seen from the observation that most of the local seismicity occurs above 60 km depth (Section 5.3). Note also that the observation network lacks resolution in deeper zones, especially below 100 km depth and along the fault margins (see Supporting Information Fig. S2). Because these areas are not our main interest, they are not further discussed.

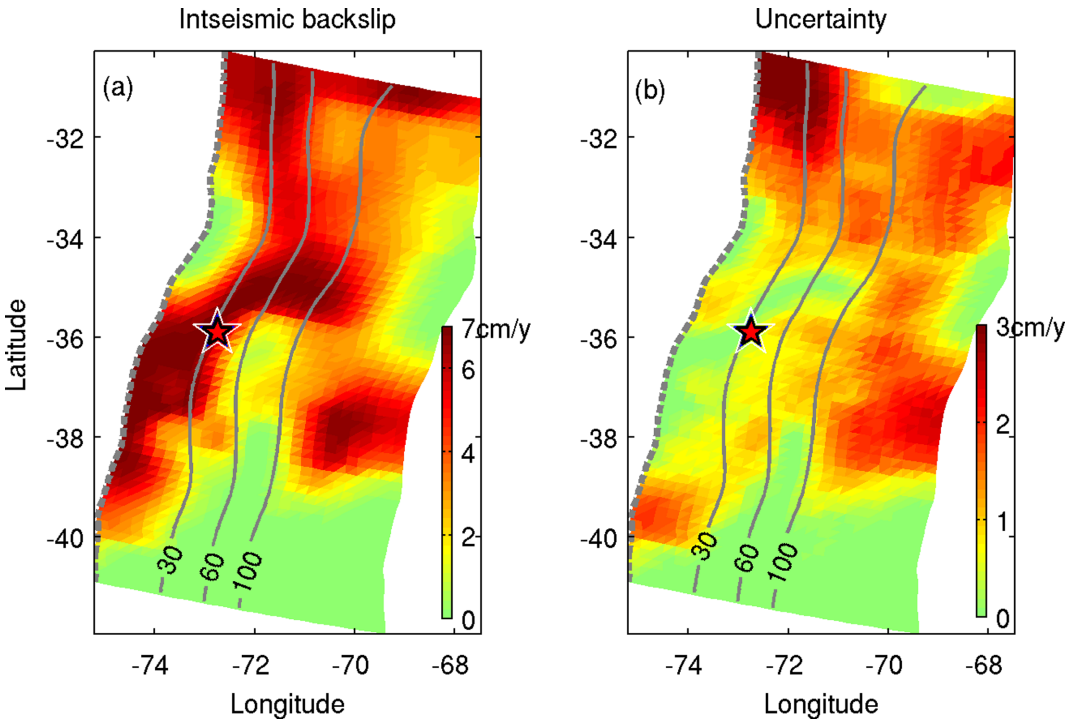

Figure 2. Colour-coded interseismic backslip rates (a) and their uncertainties (b), evaluated using the marginal PDF (see Supporting Information). The star marks the hypocentre of the 2010 M 8.8 Maule earthquake. The dashed curve marks the location of the trench and the contour lines indicate the depth levels 30, 60 and 100 km.

4.1.2 Coseismic slip model

Several coseismic modelling studies for the 2010 M 8.8 Maule earthquake have been published (Tong *et al.* 2010; Pollitz *et al.* 2011; Vigny *et al.* 2011; Moreno *et al.* 2012), using different fault geometries and inversion parameterizations. Here, we construct the coseismic slip using the model setup consistent with interseismic modelling. Our 10-fold cross-validation provides the optimal value $\lambda^2 = 0.01$ (Supporting Information Fig. S8). The modelling results (labelled Mod_1) are shown in Fig. 3 and the predicted displacement field is provided in the Supporting Information (Fig. S9). The model with a *VR* value of 96.5 per cent well reproduces the surface displacements, although the horizontal GPS measurements and InSAR are better explained than the vertical GPS measurements and land-level change data (*VR* for each data set is indicated in Supporting Information Fig. S9). This is because vertical GPS and land level change data have larger measurement errors, and thus are down-weighted in the inversion. The slip uncertainties (Fig. 3b) indicate that the slip is generally well constrained. Note that the uncertainties in this study only account for measurement errors that propagate into the slip model, but do not include other possible uncertainty sources (e.g. simplified Earth structure).

The modelled slip, resulting in a moment magnitude M_w 8.8, provides two areas of high slip: a large one north of the hypocentre and a relatively localized shallow one in the south. Comparing the inter- and coseismic modelling results (Figs 2 and 3) indicates that the 2010 Maule earthquake initiated in the area that was strongly coupled during the interseismic phase. We display in Fig. 3(a) also the contour lines for 90 per cent coupling, calculated from the interseismic backslip rate divided by the convergence rate (6.8 cm yr^{-1}). We find that a large part of the southern slip area is located in the strong coupling zone. This is not the case for the northern slip area. To further quantify the slip balance between co- and interseismic phase and to address the question whether or not, and if so to which level, the 2010 Maule earthquake filled the pre-existing seismic gap, we now construct a co- and interseismically coupled model, as presented subsequently.

4.2 Coseismic slip model constrained by interseismic coupling

4.2.1 Strain accumulation time implied by historical mega-earthquakes in the study region

Central Chile is one of the most seismically active regions of the world with several mega-earthquakes (M > 8) occurring nearly in every century. The Maule earthquake ruptured primarily the segment north of the gigantic 1960 M 9.5 event, with a small region that overlaps with the 1960 rupture. Historically recorded mega-earthquakes preceding the 1960 great earthquakes occurred in 1575, 1737 and 1837 (Abe 1981; Nishenko 1985). Therefore, the average recurrence time of mega-thrust events along the segment of the 1960 rupture has been estimated to be $\sim 128 \pm 62$ yr (Nishenko 1985). The major rupture area of the 2010 M 8.8 Maule earthquake is preceded by two historical large earthquakes in 1751 and 1835. The 1928 Talca earthquake in Maule Region with an estimated magnitude of M 7.6 (Beck *et al.* 1998; Ruegg *et al.* 2002) is far smaller than the 2010 Maule earthquake, and is not considered here. The central slip zone of the Maule earthquake ruptured in 1835 by an earthquake of M $\sim$ 8.2 (Udias *et al.* 2012; NOAA 2015). The Concepción earthquake in 1751 affected a very large region from Santiago to Valdivia, and caused a large tsunami. It has been suggested that it had a similar size and extent as the 2010 Maule earthquake (Udias *et al.* 2012; Bernhardt *et al.* 2015).

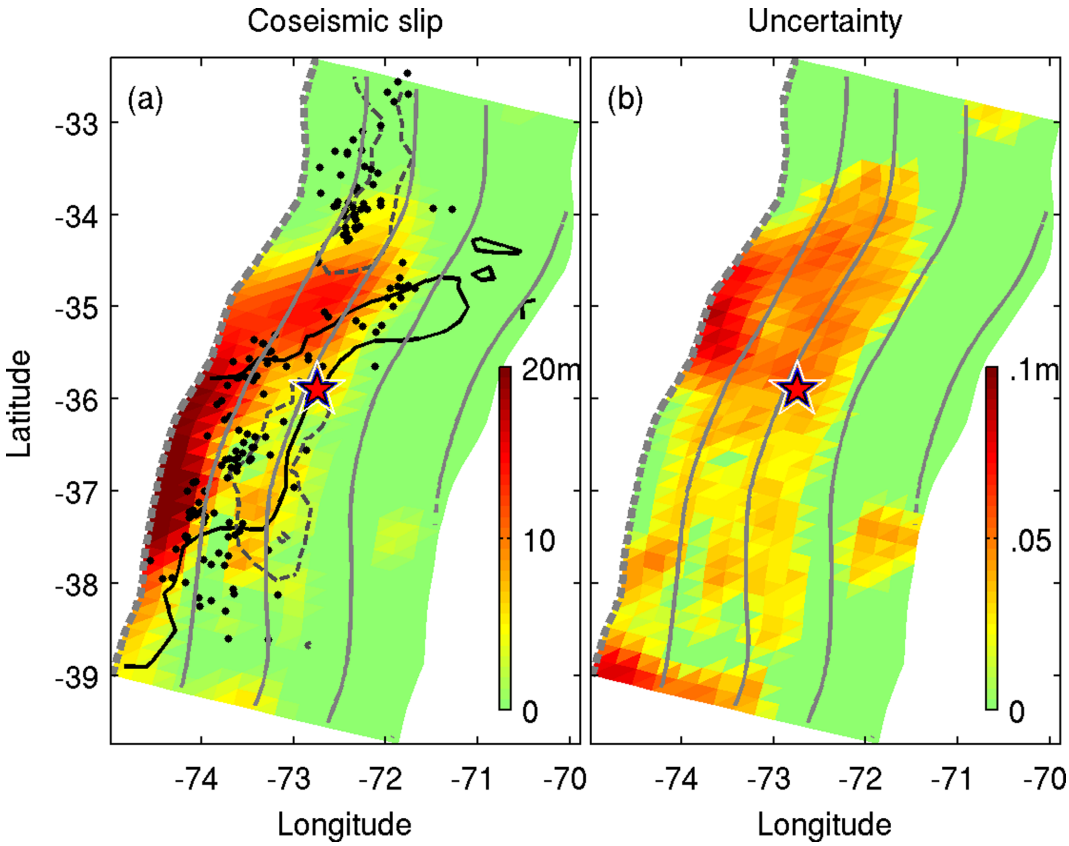

Figure 3. Colour-coded coseismic slip without interseismic constraint (a) and corresponding modelling uncertainties (b). The black-solid and black-dashed curve in panel (a) respectively marks the 90 per cent coupling derived from Fig. 2(a) and from Moreno *et al*. (2010). The star marks the hypocentre. The grey-dashed and grey-solid curves display the locations of the trench and the depth levels of 15, 30, 60 and 100 km, respectively. The black dots in panel (a) indicate aftershocks ($M \geq 5.0$, $\leq$15 km to the slab) of 2 yr following the Maule earthquake (Rietbrock *et al.* 2012). The modelled displacement fields are provided in Supporting Information Fig. S9.

Although the M$\sim$8.2 event in 1835 has possibly ruptured the central slip zone of the Maule earthquake, it is far smaller than the 2010 event (the former released only $\sim$1/18 of the seismic moment of the latter). The earthquake in 1751 has a similar size and extent as the 2010 Maule earthquake. Therefore, the longest strain accumulation time for the 2010 M 8.8 Maule earthquake is related to the occurrence of the Concepción earthquake in 1751, and thus we assume the strain accumulation time (T_r) for the 2010 Maule earthquake to be no larger than 259 yr.

4.2.2 Modelling strategy

We perform the coseismic slip inversion constrained by interseismic coupling and solve eq. (1). We constrain the coefficient **K** (equal to $T_r\boldsymbol{\kappa}$, with $0 \leq \boldsymbol{\kappa} \leq 1$) to be no larger than 259 yr, which we consider as prior information in the modelling. To keep consistent smoothing for all slip models in this study, we use $\lambda^2 = 0.01$ as above. Given λ^2, we determine γ^2 by applying a 10-fold cross-validation, and find the optimal value $\gamma^2 = 0.01$ (Supporting Information Fig S10). Noting from Supporting Information Fig. S10 that the cross-validation (CV) values are rather close for $\gamma^2 \leq 0.1$, we run the inversions with two different γ^2 values (0.01 and 0.001), and obtain identical slip models. Therefore, we adopt the optimal value $\gamma^2 = 0.01$.

We consider two types of modelling uncertainties: the uncertainty of the interseismic backslip rate (Fig. 2) and the uncertainties of the measured displacements. To account for the uncertainty in the interseismic backslip rate, we randomly pick 10 from the 1000 samples used for constructing the marginal PDFs of interseismic backslip. Concerning the measurement errors, we simulate 1000 normally distributed datasets, with mean values of the measured displacements and the standard deviations of the measurement errors. In total, 10 000 inversions are carried out for coseismic slip modelling. Based on the 10 000 modelling results, we construct the marginal PDFs for the unknowns **K**, and obtain the optimal solutions with their uncertainties. Subsequently, the optimal coseismic slip **m** (= **Kr**) and potency release level $\boldsymbol{\kappa}$ (=$\mathbf{K}/T_r$) are calculated.

4.2.3 Modelling results

We summarize our modelling results in Fig. 4, which includes the optimal coseismic slip (denoted as 'Mod_2', Fig. 4a) and its uncertainties (Fig. 4b). The inverted potency release level $\boldsymbol{\kappa}$ is shown in Fig. 4(c). The residual interseismic backslip rate (Fig. 4d) is calculated using $\mathbf{r}$-$\boldsymbol{\kappa}\mathbf{r}$, reflecting the remaining slip deficit after the Maule earthquake. We also plot the coseismic slip contour of Mod_1 in Supporting Information Fig. S2, the checkerboard test for the interseismic observation network. It indicates that the coseismic rupture of the Maule earthquake is generally in the well-resolved area of the interseismic network and thus the applied interseismic constraint is reliable.

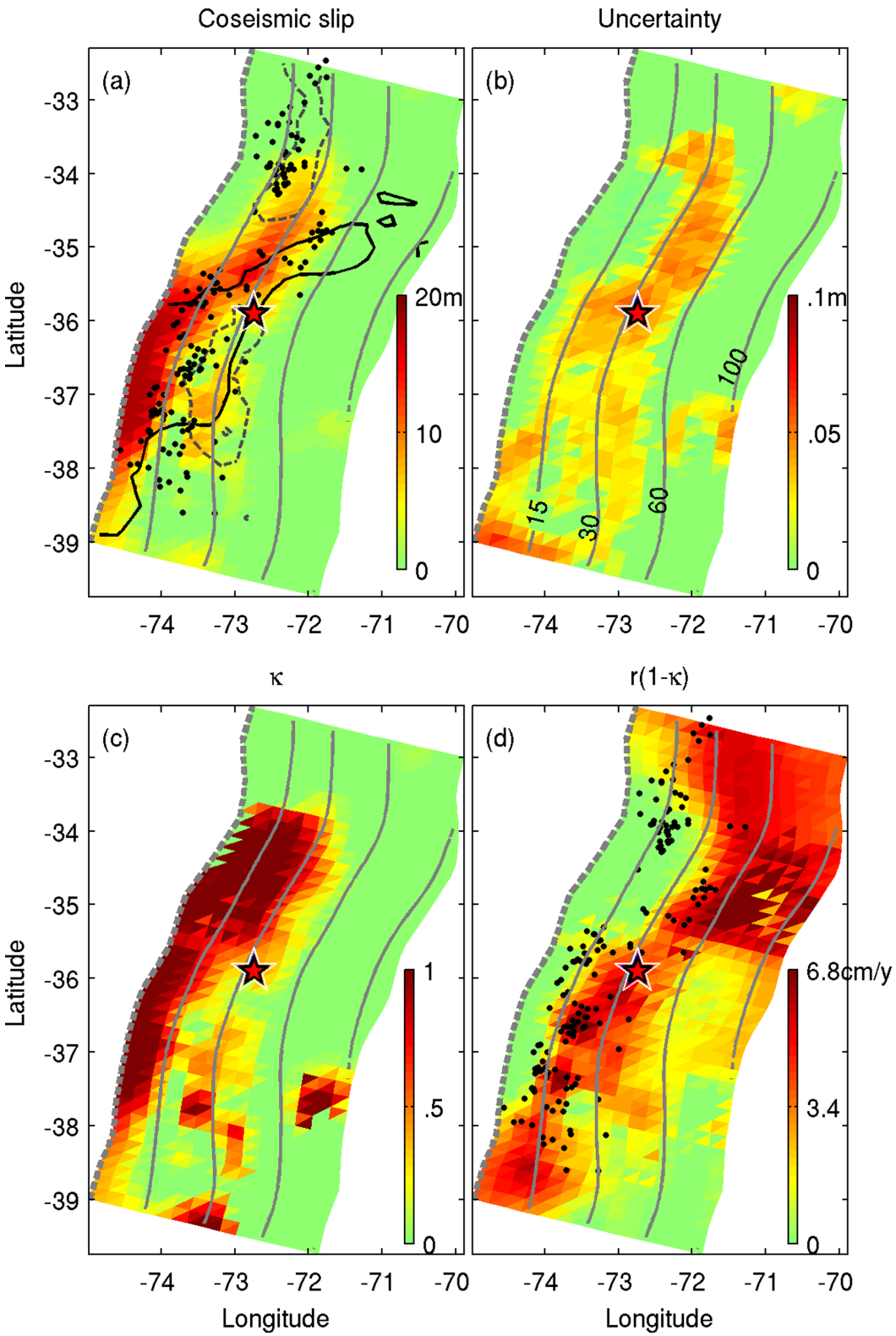

Figure 4. Colour-coded modelling results using interseismic coupling as prior (Mod_2). (a) Coseismic slip model; (b) slip uncertainty; (c) potency release level $\boldsymbol{\kappa}$; (d) residual backslip rate after the Maule earthquake (calculate by $\mathbf{r}$-$\boldsymbol{\kappa}\mathbf{r}$). Other symbols are the same as those of Fig. 3. The modelled displacement fields are provided in Supporting Information Fig. S11.

The results demonstrate that the coseismic slip models with the interseismic backslip as prior (Fig. 4) can similarly well explain the geodetic measurements as the unconstrained model (Mod_1), with slightly smaller *VR* value of 95.4 per cent, (versus 96.5 per cent of Mod_1 shown in Fig. 2a). Such consistency corroborates that the coseismic rupture of the Maule earthquake is mostly located in the interseismically coupled zone, suggesting that this large earthquake should not have come as a surprise. However, the slight degradation

of the constrained model also reflects some inconsistency between interseismic coupling and coseismic slip distribution that we will discuss in Section 5.2. Comparing Figs 4(b) and 3(b) reveals that the interseismic coupling constraint helps to slightly decrease slip uncertainty (see also Wang *et al*. 2015). The estimated **K** value for the major coseismic slip reaches the applied maximum strain accumulation time of 259 yr, and thus the relevant κ reaches 1 (see Fig. 4c), suggesting that the major coseismic slip fully released the local interseismically accumulated strain; correspondingly, the residual backslip rate is about zero after the Maule earthquake (Fig. 4d).

5 DISCUSSION

As mentioned, the non-uniqueness of fault slip inversions can bring controversial conclusions when simply comparing the inter- and coseismic slip distribution to understand the strain accumulation and release processes. We found that the predicted coseismic displacements based on a regional layered model (Lorenzo-Martín *et al.* 2006) and based on the elastic half-space are similar. Although there may exist more complex material heterogeneity (e.g. Hicks *et al.* 2014) that may affect the surface displacements locally, this will likely not influence our overall investigation based on abundance of data. Below we will show that different fault geometries, treatment of measurement uncertainties and arbitrary constraints can largely change the resolved slip distribution (in Section 5.1). Then, we quantify the inter- and coseismic slip balance based on our modelling results and evaluate the residual strain left over after the 2010 M8.8 Maule earthquake (Sections 5.1 and 5.2). The impacts from the post-seismic stress relaxation and the neighbouring mega-event, especially the 1960 M9.5 Valdivia earthquake, are addressed in Section 5.4.

5.1 Ambiguities in the slip models for the 2010 M 8.8 Maule earthquake

Whether or not the 2010 M 8.8 Maule earthquake has filled the pre-existing seismic gap has been an ongoing seismological debate, owing to inconsistent modelling strategies for inter- and coseismic slip (Moreno *et al.* 2010; Lorito *et al.* 2011) and non-uniqueness of fault slip inversion (Lay *et al.* 2010; Tong *et al.* 2010; Pollitz *et al.* 2011; Vigny *et al.* 2011; Moreno *et al.* 2012; Lin *et al*. 2013; Yue *et al.* 2014). We present some of the available coseismic slip models in Fig. 5. Visual comparison between these slip models indicates substantial differences, for example, the location of the zones of large coseismic slip. As seen, some models (Luttrell *et al.* 2011; Vigny *et al.* 2011; Yue *et al.* 2014) show largest slip above 20 km depth, similar as our modelling results, while other models (Delouis *et al.* 2010; Lorito *et al.* 2011; Pollitz *et al*. 2011) find it much deeper (between 25 and 45 km depth). Such differences have led to contrasting spatial correlation with the aftershocks locations (Rietbrock *et al.* 2012), and therefore generate ambiguities in explaining the mechanisms of aftershock triggering.

The non-uniqueness in fault slip inversion is a consequence of a variety of reasons, as pointed out above. For the depth difference of slip in the Maule earthquake, it is partially due to zero-slip constraint being arbitrarily applied at the trench in some models. Furthermore, the study based on the planar fault (Tong *et al.* 2010) indicated that a shallower dip angle (12°) of the fault results in large slip at the top edge of the fault plane. Thus, the fault geometry has a strong impact on the final slip distribution. In this study, we constrain the fault geometry using the Slab1.0 model (Hayes *et al.* 2012), and hence we expect that the modelling error related to a mismatched geometry is less significant than for a planar fault.

To further understand the causes of the slip differences, we consider here Moreno *et al.*'s model (2012) for which the same data have been used as in our study. Their inversion strategies include (1) weights to GPS, InSAR and land-level data being assigned as 0.5, 0.25 and 0.25 respectively, instead of considering the true measurement uncertainties (as in this study); (2) a zero-slip constraint at the trench and at the depth below 60 km, instead of no constraint for the two zones in our modelling; (3) variable rake angle, instead of the fixed rake angle of 112° in this study; (4) a smoothing parameter being chosen according to the balance between the smoothness of slip and data fitting quality, instead of cross-validation approach being applied in this study. We then carry out a series of fault slip inversions (Supporting Information Fig. S12) and find that the differences between Moreno's and our model can be mainly attributed to the degrees of freedom in slip and the measurement uncertainties being considered in the inversion. In comparison, our modelling involves less arbitrary constraints and considering reasonably the measurement uncertainties.

Our results indicate high strain accumulation and release near the trench. This seems to contradict to the traditional conceptual model that the upper 5–10 km of the subduction zone are overlain by an accretionary prism which undergoes significant anelastic deformation and in which earthquakes cannot nucleate (Lay & Bilek 2007). However, this view needs to be revised after the 2011 M 9 Tohoku-Oki earthquake, which generated ∼50 m of coseismic slip reaching the sea floor. Studies on rock samples recovered from the near-trench fault zone of the Tohoku-Oki earthquake also indicate that the sheared samples exhibit a variety of the fault-slip behaviours, from fast unstable slip to slow steady creep (Ikari *et al.* 2015; Hirono *et al.* 2016). Therefore, the very shallow slip in the case of the Maule earthquake is likely non-negligible, as indicated by our modelling results.

The non-uniqueness of fault slip inversion has prompted efforts to quantitatively rank inferred slip models for an event (e.g. for the 2011 M 9 Tohoku-Oki earthquake, Brown *et al.* 2015; Razafindrakoto *et al.* 2015). The uncertainty in slip inversions is also a concern when evaluating strain accumulation and release during the seismic cycle. We therefore conduct the inversion with additional physical considerations to quantify the slip balance based on a consistent model setup for both inter- and coseismic phases, with the goal to address the question if and how the 2010 M 8.8 Maule earthquake released the strain accumulated during the interseismic phase.

We also evaluate an alternative interseismic coupling model (Moreno *et al.* 2010) that has frequently been used in evaluating the regional seismic hazard (e.g. Lorito *et al.* 2011; Moreno *et al.* 2012). We display the 90 per cent coupling of Moreno's model in Figs 3(a) and 4(a) by dashed contours, showing significant deviations from our model (solid contour lines) possibly due to differences in the adopted fault geometry and the modelling strategy. We also test a coseismic slip model constrained by Moreno's inferred coupling. The results are shown in Supporting Information Fig. S14, indicating that the derived coseismic slip is to first order similar to Mod_2 (Fig. 4a), but the strongest slip is located north of the hypocentre. This indicates that the interseismic constraint influences the final coseismic slip distribution, and further impacts our understanding of regional strain accumulation and release process.

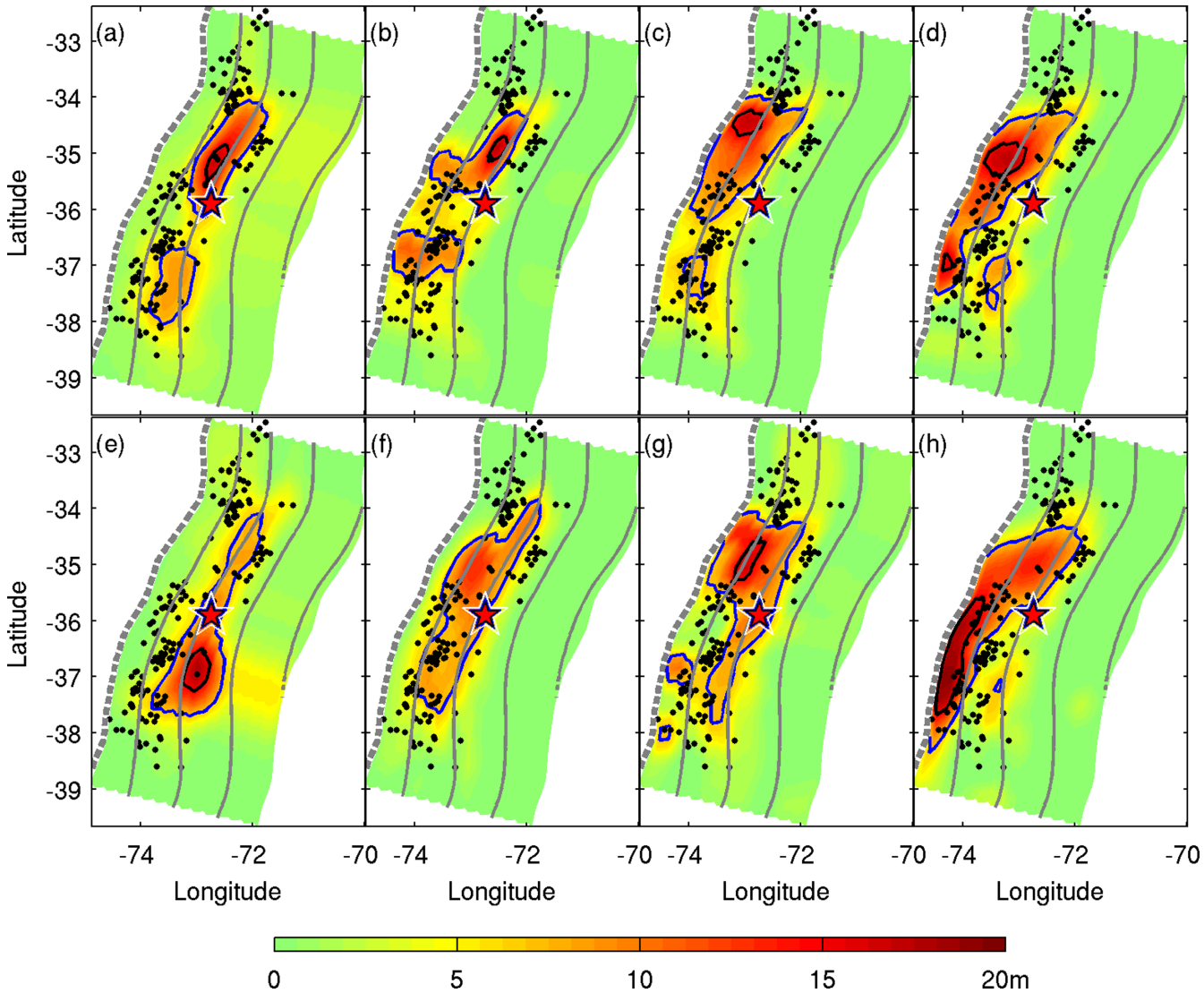

Figure 5. Published coseismic slip models: (a) Lorito *et al.* (2011)—based on Tsunami, continuous GPS and InSAR data , (b) Delouis *et al.* (2010)—based on static and high-rate GPS, InSAR and broad-band teleseismic data, (c) Luttrell *et al.* (2011)—based on GPS and InSAR data, (d) Vigny *et al.* (2011)—based on GPS data, (e) Pollitz *et al.* (2011)—based on GPS and InSAR data, (f) Moreno *et al.* (2012)—based on GPS, InSAR and land-level changes data, (g) Yue *et al.* (2014)—based on high-rate GPS, teleseismic body waves, InSAR, campaign GPS and tsunami observations and (h) this study—based on GPS, InSAR and land-level changes data.

5.2 Slip-balance between inter- and coseismic phase

As mentioned above, non-uniqueness exists in both co- and interseismic slip inversion. Particularly, previous studies compared the coseismic rupture with the interseismic coupling distribution derived from different model setups. In this study, we model inter- and coseismic slip self-consistently, and investigate their slip-balance. Overall, our modelling results reveal that: (1) the 2010 Maule earthquake initiated in the strong coupling zone, indicated by its hypocentre being located in the area of high backslip (Fig. 2a); (2) the large coseismic slip south of the hypocentre is located in the strong interseismic coupling zone, and the strain release is possibly complete, which is manifested by the residual strain of about zero after the Maule earthquake (above the 15 km depth). However, below the southern slip zone at the depth of 15–40 km, the remaining strain is still significant; (3) the coseismic slip north of the hypocentre is strong, but falls within a weak coupling zone (Fig. 2a).

We also remark that the northern coseismic rupture observed in Mod_1 is not well resolved in Mod_2, whose data fitting level is also lower than Mod_1 (by $\sim$1 per cent), as seen in Supporting Information Fig. S11a. Trying to explain the residual displacements $\Delta\mathbf{d}_2$ ($\Delta\mathbf{d}_2 = \mathbf{d} - \mathbf{d}_2$, with $\mathbf{d}$ being the observations and $\mathbf{d}_2$ being the modelled displacements of Mod_2) using the model setup identical to Mod_1 (without interseismic constraint), we find that residual displacements $\Delta\mathbf{d}_2$ requires an additional slip of $\sim$6 m (see Fig. 6, labelled as '$\Delta\mathrm{Mod}_2$'). $\Delta\mathrm{Mod}_2$ can improve the data fitting by $\sim$1 per cent, and Mod_2 together with $\Delta\mathrm{Mod}_2$ can similarly explain the data as Mod_1. The results indicate that the Maule earthquake locally released more potency than that accumulated since the last mega-event in 1751.

The extra release of slip potency beyond that interseismically accumulated could imply that considerable strain was left behind after the 1751 earthquake, hence, strain started to build up from a non-zero state in the slip area of $\Delta\mathrm{Mod}_2$. On the other hand, the extra slip of $\Delta\mathrm{Mod}_2$ might be due to dynamic overshoot during

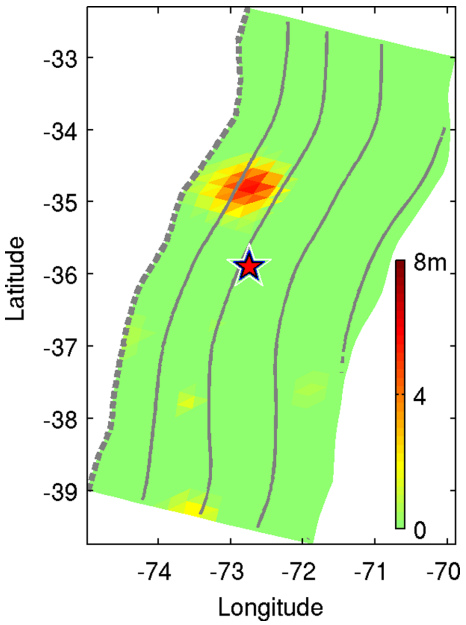

Figure 6. Fault slip inverted from the residual displacements (the difference between the observed and modelled displacements of Mod_2) without interseismic constraint, named as ΔMod_2. The other symbols are the same as those in Fig. 3.

the coseismic rupture of the 2010 Maule earthquake, as suggested by normal faulting aftershocks near this slip zone (Rietbrock *et al.* 2012) and also inferred from mechanical analysis (Cubas *et al.* 2013).

5.3 To which level did the Maule earthquake fill the seismic gap?

Our modelling results imply that slip potency is likely still significant even after the occurrence of the 2010 M 8.8 Maule earthquake, indicated by the high residual backslip rate (Fig. 4d). Following Wang *et al*. (2015), we calculate the overall potency release level (α) in terms of accumulation and release of slip potency. For the interseismic phase, we consider the backslip rate, while the slip rate contributing to the main shock is quantified by $\boldsymbol{\kappa r}$. Given that the slip area is constant in this calculation, the ratio of slip potency can be simply measured by ratio of slip rate (Wang *et al.* 2015)

$$\alpha = \frac{\sum \kappa r}{\sum r}. \tag{3}$$

Here we focus on the fault area above 60 km depth, where more than 80 per cent of earthquakes in this region occur (see Supporting Information Fig. S15), and which is also close to the continental Moho depth (according to Crust 5.1, Mooney *et al.* 1998). Hence, we also ignore the deeper parts of the fault for which the resolution of the interseismic network is poor. The bounding areas outside of the major coseismic rupture zone of the Maule earthquake overlap partially with the 1960 M 9.5 great Valdivia earthquake in the south, and two earthquakes that occurred in the north in 1985 (M 8.0) and 1906 (M 8.4) (see Fig. 1), and should be excluded from the calculation.

The calculated α-value is about ∼45 per cent for the region above 60 km depth (Fig. 4d), but increases to ∼53 per cent or ∼55 per cent if we further focus on the major coseismic rupture zone between 34°S and 38°S or the hypothesized seismic gap between 35°S and 37°S (Ruegg *et al.* 2009). Thus, our modelling results show that the 2010 M 8.8 Maule main shock released about ∼55 per cent of the accumulated strain energy of the seismic gap.

It is apparent that there is a localized zone of remaining strain south of the hypocentre, approximately at the depth level of ∼15–40 km and between 35.5°S and 37°S. Taking the strain accumulation time of 259 yr, the remaining slip deficit is equivalent to an ∼M 8.4 earthquake.

5.4 Roles of the 1960 M 9.5 Valdivia earthquake and the post-seismic relaxation processes

We have focused only on the inter- and coseismic phase so far. We now discuss the impact of surrounding strong earthquakes and the post-seismic relaxation processes of the 2010 Maule earthquake. Both may produce stress changes, and trigger/discourage the regional seismicity (e.g. Toda & Stein 2000). We first analyse the 1960 M 9.5 Valdivia earthquake, which marks the southern border of the seismic gap (see Fig. 1), but ignore two earthquakes that occurred in 1985 (M 8.0) and 1906 (M 8.4) north of the seismic gap, whose moment releases is much smaller than for 2010 (less than 10 per cent) and 1960 (less than 5 per cent) events. Next, we investigate how the post-seismic relaxation processes of the 2010 Maule earthquake may influence the slip-balance during the seismic cycle.

We utilize a simple slip model for the 1960 M 9.5 Valdivia earthquake and a layered viscoelastic medium calibrated by the modern GPS measurements (Lorenzo-Martín *et al.* 2006). We calculate the shear stress changes (along the rake angle of 112°) on the fault for the Maule earthquake, produced by the 1960 Valdivia main shock and its post-seismic viscoelastic relaxation over 50 yr. The results in Fig. 7 indicate that the southern part of the rupture area of the Maule earthquake, particularly near its hypocentre, was loaded by this mega-earthquake both co- and post- seismically, suggesting the occurrence of the 2010 Maule event may have been advanced by the 1960 Valdivia earthquake. The total stress increase at the hypocentre of the Maule earthquake is about 0.06 MPa, equivalent to the effect of ∼9 yr of tectonic loading (0.007 MPa yr^{-1} calculated from slip rate of Fig. 2a).

Using the same layered viscoelastic medium as that for the Valdivia earthquake, we calculate the post-seismic viscoelastic relaxation of the 2010 Maule earthquake. The results (Fig. 8b) display that the deep viscoelastic relaxation plays a role to rebuild the stress in the seismogenic zone. For comparison, we also plot the coseismic stress change (Fig. 8a) and the stress rate calculated from Fig. 4(d) (Fig. 8c). The stress buildup over 7 yr after the Maule earthquake due to deep viscoelastic relaxation is equivalent to ∼8 yr of tectonic loading at the Maule hypocentre, and it decays exponentially (Savage & Prescott 1978) or logarithmically (Shen *et al.* 1994) with time. Therefore, both the Valdivia earthquake and the post-seismic viscoelastic relaxation of the Maule earthquake cause stress increase in the targeted seismic gap. They are equivalent to about 20 yr of tectonic loading at the Maule hypocentre. Since these overall stress changes are localized (e.g. the Valdivia earthquake only impacted the southern end of the coseismic Maule rupture) and small compared to the total strain buildup in the interseismic phase, we do not specifically include the two components into the calculation of slip-balance, although they apparently increase the local strain.

Studies indicate that afterslip of the Maule earthquake concentrates at the downdip end of the coseismic rupture zone, at depths of ∼30–60 km (Bedford *et al.* 2013; Lin *et al.* 2013), where the

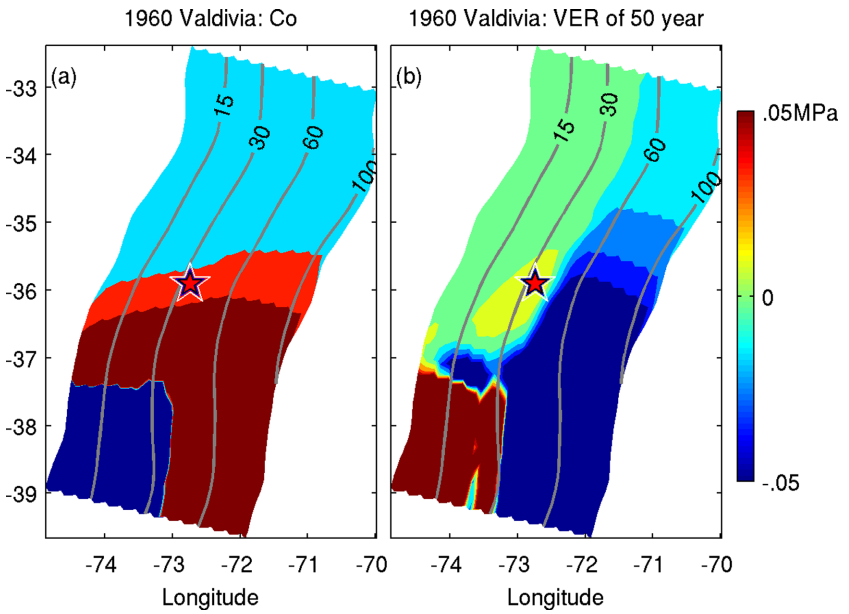

Figure 7. Shear stress changes along the rake angle of 112° produced by the 1960 M 9.5 Valdivia earthquake (a) and its post-seismic viscoelastic relaxation (VER) over 50 yr (b).

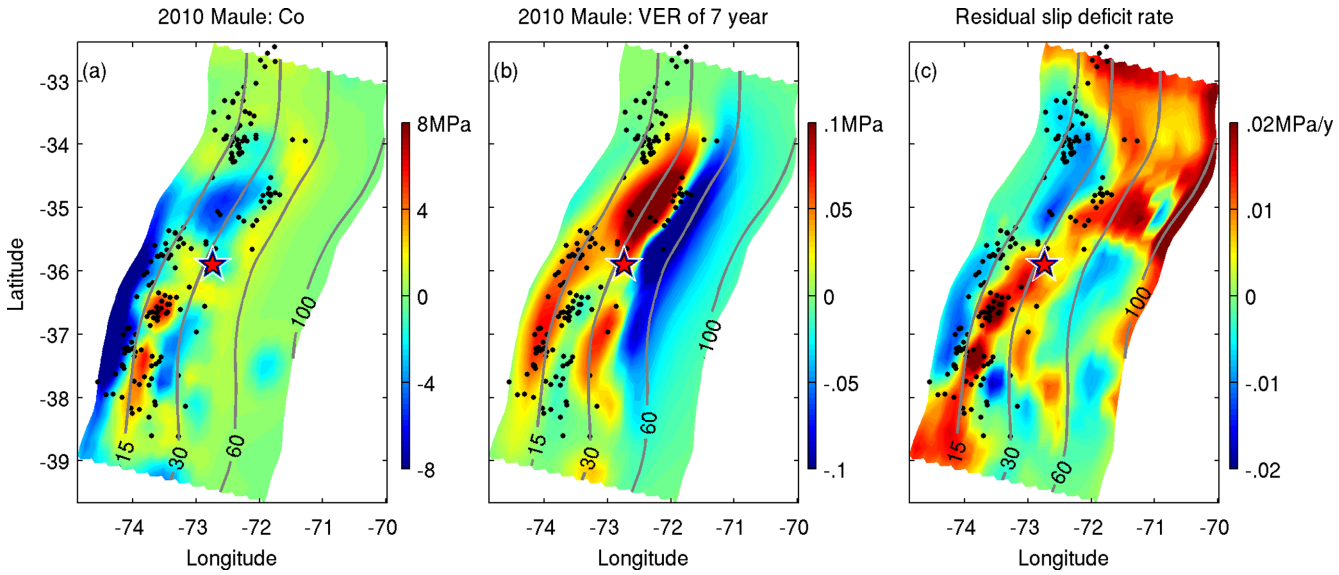

Figure 8. Shear stress changes due to coseismic slip of Mod_1 (a), deep viscoelastic relaxation (VER) over 7 yr after the Maule earthquake (b) and residual slip deficit rate according to Fig. 4(d) (c).

remaining strain is still high after the Maule earthquake (see Fig. 4d). It suggests that a large part of remaining strain at this depth was likely released in the mode of aseismic slip. The afterslip that occurred over 1.3 yr released slip potency equivalent to ∼20–30 per cent of that released by the main shock (Lin *et al.* 2013). These data on the post-seismic phase were not available in previous studies that addressed the question of the seismic gap (Moreno *et al.* 2010; Lorito *et al.* 2011; Moreno *et al.* 2012). Therefore, combining the main shock and the post-seismic afterslip (by 55 per cent × $(1 + q)$, with q being ∼20–30 per cent for aseismic relaxation), the strain release of the Maule earthquake is approximately 67–72 per cent of the regional strain accumulated since the last big earthquake in 1751.

We display the aftershocks ($M \geq 5.0$, distance ≤15 km to the slab) recorded within 2 yr after the Maule earthquake (Rietbrock *et al.* 2012) in Fig. 8 and Figs 3–5, overlying the coseismic slip distribution. The seismic moment release of these aftershocks is almost negligible, accounting for only about 1.2 per cent of the main-shock moment release. Most of the aftershocks, except the ones near the northern slip that show a normal faulting mechanism, are located in areas in which either coseismic stress drop was high, but was loaded post-seismically (e.g. by viscoelastic relaxation shown in Fig. 8b) or in areas in which a slip deficit remained after the Maule earthquake (Fig. 8c) and is also loaded by coseismic stress perturbations (Fig. 8a). They indicate that the aftershocks were triggered by the stress changes produced by both the main shock and its post-seismic aseismic relaxation, and further released the interseismically accumulated strain.

In the area in which the remaining strain is still high after the Maule earthquake (latitude of ∼35.5°S–37°S and depth of

~15–40 km), aftershocks are abundant (see Fig. 4d). We calculate that the seismic moment released by these aftershocks is equivalent to an M 7.2 earthquake, much smaller than the preserved strain energy for an M 8.4 event. The published afterslip appears also to be mainly concentrated at the deeper depth (Bedford *et al.* 2013; Lin *et al.* 2013). Furthermore, the 1960 Valdivia earthquake leads to stress increase in this area. Therefore, the remaining strain south of the hypocentre, at the depth of 15–40 km, possibly remains high enough for an M 8.4 earthquake.

6 CONCLUSIONS

This study applies the inversion approach of Wang *et al*. (2015) to quantify the slip balance during the seismic cycle for understanding whether or not the 2010 M 8.8 Maule earthquake has filled the pre-existing seismic gap. Using a fault model constructed based on the subduction-zone geometry of Slab 1.0, we demonstrate that the Maule earthquake and its post-seismic slip over 1.3 yr released ~67–72 per cent of the strain accumulated since the last big earthquake in 1751 in this region. Based on our modelling, the remaining strain after the Maule earthquake is concentrated mainly south of the hypocentre and has the slip potency equivalent to an M 8.4 earthquake, considering a strain accumulation time of 259 yr. In contrast, the coseismic slip north of the hypocentre released potency higher than the amount accumulated since 1751, suggesting likely dynamic over-shoot of the Maule earthquake or that the last mega-event in 1751 did not fully release the local strain so that the strain started to build up from a non-zero state.

We point out that fault slip inversions generally suffer from non-uniqueness, owing to effects of limited data (and their processing and utilization) and their measurement errors, unmodelled Earth structure, imprecisely known fault geometry, variable inversion parameterizations, as well as differences in treating the forward problem. Therefore, it is difficult to unambiguously quantify the slip balance between the different stages of strain accumulation and strain release based only on the spatial distributions of the inverted slip models. Future work needs to include these uncertainties and incorporate them, ideally in a Bayesian framework, to help to fully answer the question whether or not the Maule earthquake filled the seismic gap.

ACKNOWLEDGEMENTS

We thank Gavin Hayes and another anonymous reviewer for their constructive, profound and detailed comments that greatly improve our work. This research was supported by NSFC-41674067, projects of State Key Laboratory of Earthquake Dynamics LED2015A02 and LED2016A05, and also partially supported by King Abdullah University of Science and Technology (KAUST) in Thuwal, Saudi Arabia, grant BAS/1/1339-01-01.

REFERENCES

Abe, K., 1981. Magnitudes of large shallow earthquakes from 1904 to 1980, *Phys. Earth planet. Inter.*, **27,** 72–92.

Beck, S., Barrientos, S., Kausel, E. & Reyes, M., 1998. Source characteristics of historic earthquakes along the central Chile subduction zone, *J. South Am. Earth Sci.*, **11,** 115–129.

Bedford, J. *et al.*, 2013. A high-resolution, time-variable afterslip model for the 2010 Maule M_w = 8.8, Chile megathrust earthquake, *Earth planet. Sci. Lett.*, **383,** 26–36.

Bernhardt, A., Melnick, D., Hebbeln, D., Lückge, A. & Strecker, M.R., 2015. Turbidite paleoseismology along the active continental margin of Chile – Feasible or not?, *Quat. Sci. Rev.*, **120,** 71–92.

Brietzke, G.B., Cochard, A. & Igel, H., 2009. Importance of bimaterial interfaces for earthquake dynamics and strong ground motion, *Geophys. J. Int.*, **178,** 921–938.

Brown, L., Wang, K. & Sun, T., 2015. Static stress drop in the M_w 9 Tohoku-oki earthquake: heterogeneous distribution and low average value, *Geophys. Res. Lett.*, **42,** 10 595–10 600.

Campos, J. *et al.*, 2002. A seismological study of the 1835 seismic gap in south-central Chile, *Phys. Earth planet. Inter.*, **132,** 177–195.

Cubas, N., Avouac, J., Souloumiac, P. & Leroy, Y., 2013. Megathrust friction determined from mechanical analysis of the forearc in the Maule earthquake area, *Earth planet. Sci. Lett.*, **381,** 92–103.

Delouis, B., Nocquet, J.-M. & Vallée, M., 2010. Slip distribution of the February 27, 2010 $M_w = 8.8$ Maule Earthquake, central Chile, from static and high-rate GPS, InSAR, and broadband teleseismic data, *Geophys. Res. Lett.*, **37,** L17305, doi:10.1029/2010GL043899.

Du, Y., Aydin, A. & Segall, P., 1992. Comparison of various inversion techniques as applied to the determination of a geophysical deformation model for the 1983 Borah Peak earthquake, *Bull. seism. Soc. Am.*, **82,** 1840–1866.

Gomez, F. *et al.*, 2007. Global Positioning System measurements of strain accumulation and slip transfer through the restraining bend along the Dead Sea fault system in Lebanon, *Geophys. J. Int.*, **168,** 1021–1028.

Hayes, G.P., Wald, D.J. & Johnson, R.L., 2012. Slab1.0: a three-dimensional model of global subduction zone geometries, *J. geophys. Res.*, **117,** B01302, doi:10.1029/2011JB008524.

Herrmann, L.R., 1976. Laplacian-isoparametric grid generation scheme, *J. Eng. Mech. Div.*, **102,** 749–756.

Hicks, S.P., Rietbrock, A., Ryder, I.M.A., Lee, C.-S. & Miller, M., 2014. Anatomy of a megathrust: The 2010 M8.8 Maule, Chile earthquake rupture zone imaged using seismic tomography, *Earth planet. Sci. Lett.*, **405,** 142–155.

Hirono, T., Tsuda, K., Tanikawa, W., Ampuero, J.-P., Shibazaki, B., Kinoshita, M. & Mori, J.J., 2016. Near-trench slip potential of megaquakes evaluated from fault properties and conditions, *Sci. Rep.*, **6,** doi:10.1038/srep28184.

Ikari, M.J., Ito, Y., Ujiie, K. & Kopf, A.J., 2015. Spectrum of slip behaviour in Tohoku fault zone samples at plate tectonic slip rates, *Nat. Geosci.*, **8,** 870–874.

Jónsson, S., Zebker, H., Segall, P. & Amelung, F., 2002. Fault slip distribution of the M_w 7.1 Hector Mine, California, earthquake, estimated from satellite radar and GPS measurements, *Bull. seism. Soc. Am.*, **92,** 1377–1389.

Jordan, T.H., 2006. Earthquake predictability, brick by brick, *Seismol. Res. Lett.*, **77,** 3–6.

Klotz, J., Khazaradze, G., Angermann, D., Reigber, C., Perdomo, R. & Cifuentes, O., 2001. Earthquake cycle dominates contemporary crustal deformation in Central and Southern Andes, *Earth planet. Sci. Lett.*, **193,** 437–446.

Lay, T. & Bilek, S., 2007. Anomalous earthquake ruptures at shallow depths on subduction zone megathrusts, in *The Seismogenic Zone of Subduction Thrust Faults*, pp. 476–511, eds Dixon, T.H. & Moore, J.C., Columbia Univ. Press.

Lay, T., Ammon, C.J., Kanamori, H., Koper, K.D., Sufri, O. & Hutko, A.R., 2010. Teleseismic inversion for rupture process of the 27 February 2010 Chile (M_w 8.8) earthquake, *Geophys. Res. Lett.*, **37,** L13301, doi:10.1029/2010GL043379.

Lin, Y.-N.N. *et al.*, 2013. Coseismic and postseismic slip associated with the 2010 Maule earthquake, Chile: characterizing the Arauco Peninsula barrier effect, *J. geophys. Res.*, **118**(6), 3142–3159.

Lohman, R. & Simons, M., 2005. Some thoughts on the use of InSAR data to constrain models of surface deformation: noise structure and data downsampling, *Geochem. Geophys. Geosyst.*, **6,** Q01007, doi:10.1029/2004GC000841.

Lorenzo-Martín, F., Roth, F. & Wang, R., 2006. Inversion for rheological parameters from post-seismic surface deformation associated with the 1960 Valdivia earthquake, Chile, *Geophys. J. Int.*, **164,** 75–87.

Lorito, S. *et al.*, 2011. Limited overlap between the seismic gap and coseismic slip of the great 2010 Chile earthquake, *Nature*, **4,** 173–177.

Luttrell, K.M., Tong, X., Sandwell, D.T., Brooks, B.A. & Bevis, M.G., 2011. Estimates of stress drop and crustal tectonic stress from the 27 February 2010 Maule, Chile, earthquake: implications for fault strength, *J. geophys. Res.*, **116,** B11401, doi:10.1029/2011JB008509.

Mai, P.M. & Thingbaijam, K.K.S., 2014. SRCMOD: an online database of finite-fault rupture models, *Seismol. Res. Lett.*, **85,** 1348–1357.

Mai, P.M. *et al.*, 2016. The Earthquake-source inversion validation (SIV) project, *Seismol. Res. Lett.*, **87,** 690–708.

McCann, W.R., Nishenko, S.P., Sykes, L.R. & Krause, J., 1979. Seismic gaps and plate tectonics: seismic potential for major boundaries, *Pure appl. Geophys.*, **117,** 1082–1147.

McGuire, J.J., 2008. Seismic cycles and Earthquake predictability on east pacific rise transform faults, *Bull. seism. Soc. Am.*, **98,** 1067–1084.

Meade, B.J., 2007. Algorithms for the calculation of exact displacements, strains, and stresses for triangular dislocation elements in a uniform elastic half space, *Comput. Geosci.*, **33,** 1064–1075.

Melnick, D., Cisternas, M., Moreno, M. & Norambuena, R., 2012. Estimating coseismic coastal uplift with an intertidal mussel: calibration for the 2010 Maule Chile earthquake ($M_w = 8.8$), *Quat. Sci. Rev.*, **42,** 29–42.

Metois, M., Socquet, A. & Vigny, C., 2012. Interseismic coupling, segmentation and mechanical behavior of the central Chile subduction zone, *J. Geophys. Res.*, **117,** B03406, doi:10.1029/2011JB008736.

Mooney, W.D., Laske, G. & Masters, T.G., 1998. CRUST 5.1: A global crustal model at $5^\circ \times 5^\circ$, *J. geophys. Res.*, **103,** 727–747.

Moreno, M., Klotz, J., Melnick, D., Echtler, H. & Bataille, K., 2008. Active faulting and heterogeneous deformation across a megathrust segment boundary from GPS data, south central Chile (36–39°S), *Geochem. Geophys. Geosyst.*, **9,** 1–14.

Moreno, M., Rosenau, M. & Oncken, O., 2010. 2010 Maule earthquake slip correlates with pre-seismic locking of Andean subduction zone, *Nature*, **467,** 198–202.

Moreno, M. *et al.*, 2012. Toward understanding tectonic control on the M_w 8.8 2010 Maule Chile earthquake, *Earth planet. Sci. Lett.*, **321–322**, 152–165.

Nishenko, S.P., 1985. Seismic potential for large and great interplate earthquakes along the Chilean and Southern Peruvian Margins of South America: a quantitative reappraisal, *J. geophys. Res.*, **90,** 3589–3615.

NOAA, 2015. National Geophysical Data Center/World Data Service (NGDC/WDS), Global Significant Earthquake Database, National Geophysical Data Center.

Okada, Y., 1985. Surface deformation due to shear and tensile faults in a half-space, *Bull. seism. Soc. Am.*, **75,** 1135–1154.

Pacheco, J.F., Sykes, L.R. & Scholz, C.H., 1993. Nature of seismic coupling along simple plate boundaries of the subductiontype, *J. geophys. Res.*, **98,** 14 133–14 159.

Page, M., Custodio, S., Archuleta, R. & Carlson, J.M., 2009. Constraining earthquake source inversions with GPS data: 1. Resolution-based removal of artifacts, *J. geophys. Res.*, **114,** B01314, doi:10.1029/2007JB005449.

Perfettini, H., Avouac, J., Tavera, H., Kositsky, A. & Nocquet, J., 2010. Seismic and aseismic slip on the Central Peru megathrust, *Nature*, **465,** 78–81.

Peterson, E.T. & Seno, T., 1984. Factors a¡ecting seismic moment release rates in subduction zones, *J. geophys. Res.*, **89,** 10 233–10 248.

Pollitz, F. *et al.*, 2011. Coseismic slip distribution of the February 27, 2010 M_w8.8 Maule, Chile earthquake, *Geophys. Res. Lett.*, **38,** L09309, doi:10.1029/2011GL047065.

Razafindrakoto, H.N.T., Mai, P.M., Genton, M.G., Zhang, L. & Thingbaijam, K.K.S., 2015. Quantifying variability in earthquake rupture models using multidimensional scaling: application to the 2011 Tohoku earthquake, *Geophys. J. Int.*, **202,** 17–40.

Reid, H.F., 1910. Elastic rebound theory, *Bull. Dept. Geol. Sci.*, **6,** 413–433.

Rietbrock, A., Ryder, I., Hayes, G., Haberland, C., Comte, D., Roecker, S. & Lyon-Caen, H., 2012. Aftershock seismicity of the 2010 Maule $M_w = 8.8$, Chile, earthquake: correlation between co-seismic slip models and aftershock distribution?, *Geophys. Res. Lett.,* **39,** L08310, doi:10.1029/2012GL051308.

Ruegg, J.C. *et al.*, 2002. Interseismic strain accumulation in south central Chile from GPS measurements, 1996–1999, *Geophys. Res. Lett.*, **29,** 12-11–12-14.

Ruegg, J.C. *et al.*, 2009. Interseismic strain accumulation measured by GPS in the seismic gap between Constitucion and concepcion in Chile, *Phys. Earth planet. Inter.*, **175,** 78–85.

Ruff, L. & Kanamori, H., 1980. Seismicity and the subduction process, *Phys. Earth planet. Inter.*, **23,** 240–252.

Savage, J.C., 1983. A dislocation model of strain accumulation and release at a subduction zone, *J. geophys. Res.*, **88,** 4984–4996.

Savage, J.C. & Prescott, W.H., 1978. Asthenosphere readjustment and the earthquake cycle, *J. geophys. Res.*, **83,** 3369–3376.

Scholz, C.H. & Small, C., 1997. The effect of seamount subduction on seismic coupling, *Geology*, **25,** 487–490.

Shen, Z.-K., Jackson, D.D., Feng, Y., Cline, M., Kim, M., Fang, P. & Bock, Y., 1994. Postseismic deformation following the Landers earthquake, California, 28 June 1992, *Bull. seism. Soc. Am.*, **84,** 780–791.

Storchak, D.A., Di Giacomo, D., Bondár, I., Engdahl, E.R., Harris, J., Lee, W.H.K., Villaseñor, A. & Bormann, P., 2013. Public release of the ISC–GEM Global Instrumental Earthquake Catalogue (1900–2009), *Seismol. Res. Lett.*, **84,** 810–815.

Sykes, L.R. & Menke, W., 2006. Repeat times of large Earthquakes: implications for Earthquake mechanics and long-term prediction, *Bull. seism. Soc. Am.*, **96,** 1569–1596.

Toda, S. & Stein, R., 2000. Did stress triggering cause the large off-fault aftershocks of the 25 March 1998 $M_w = 8.1$ Antarctic plate earthquake?, *Geophys. Res. Lett.*, **27,** 2301–2304.

Tong, X. *et al.*, 2010. The 2010 Maule, Chile earthquake: downdip rupture limit revealed by space geodesy, *Geophys. Res. Lett.*, **37,** L24311, doi:10.1029/2010GL045805.

Udias, A., Madariaga, R., Buforn, E., Munoz, D. & Ros, M., 2012. The large Chilean historical earthquakes of 1647, 1657, 1730, and 1751 from contemporary document, *Bull. seism. Soc. Am.*, **102,** 1639–1653.

Vigny, C. *et al.*, 2011. The 2010 M_w 8.8 Maule mega-thrust earthquake of Central Chile, monitered by GPS, *Science*, **332,** 1417–1421.

Wang, K., Hu, Y. & He, J., 2012a. Deformation cycles of subduction earthquakes in a viscoelastic Earth, *Nature*, **484,** 327–332.

Wang, L., Hainzl, S., Zöller, G. & Holschneider, M., 2012b. Stress- and aftershock-constrained joint inversions for co- and post-seismic slip applied to the 2004 M6.0 Parkfield earthquake, *J. geophys. Res.*, **117,** B07406, doi:10.1029/2011JB009017.

Wang, L., Hainzl, S. & Mai, P.M., 2015. Quantifying slip balance in the earthquake cycle: coseismic slip model constrained by interseismic coupling, *J. geophys. Res.*, **120,** 8383–8403.

Wells, D.W. & Coppersmith, K.J., 1994. New empirical relationships among magnitude, rupture length, rupture width, rupture area, and surface displacement, *Bull. seism. Soc. Am.*, **84,** 974–1002.

Yue, H., Lay, T., Rivera, L., An, C., Vigny, C., Tong, X. & Báez Soto, J.C., 2014. Localized fault slip to the trench in the 2010 Maule, Chile $M_w = 8.8$ earthquake from joint inversion of high-rate GPS, teleseismic body waves, InSAR, campaign GPS, and tsunami observations, *J. geophys. Res.*, **119,** 7786–7804.

SUPPORTING INFORMATION

Supplementary data are available at *GJI* online.

Figure S1. Variance reduction as function of the rake angle of the slip vector. The triangles mark the models with the largest variance reduction value.

Figure S2. Checkerboard test for the inversion approach and the utilized GPS network for interseismic modelling: (a) Synthetic (slip of 1 meter at the sites marked with dots, and 0 m slip otherwise) and modelled (colour-coded) slip; (b) colour-coded slip uncertainties; (c) grid-search results for different λ^2 based on cross-validation approach; marginal PDFs of slip at the fault patch '+' marked in

panel (b) are shown respectively in panels (d) and (e). The stars in panels (a) and (b) indicate the hypocentre of the 2010 M 8.8 Maule earthquake, the grey dashed curve marks the location of trench and the contour lines indicate 30, 60 and 100 km depth levels. The black dashed contour indicates the 5-m coseismic slip of Mod_1.

Figure S3. The synthetic displacements (black arrows) and the modelling residuals (red arrows) for the checkerboard test shown in Fig. S2(a). The dark-grey dots display the applied fault plane for coseismic modelling, while the light-grey dots show the fault plane for interseismic modelling. The thick dashed line marks the location of the trench.

Figure S4. Checkerboard test for the inversion approach using continuous GPS measurements for the coseismic phase. (a) Synthetic (slip of 1 meter at the sites marked with dots and 0 m slip otherwise) and modelled (colour-coded) slip; (b) colour-coded uncertainties of the inverted slip; synthetic (black arrows) and modelling residuals (red arrows) of the surface displacements are shown in panels (c) and (d), in which the grey dots mark the fault plane for coseismic modelling. The star marks the hypocentre of the Maule earthquake. The dashed curve marks the location of trench and the grey-solid curves indicate the depth levels of 15, 30, 60 and 100 km.

Figure S5. Similar to Figs S4(a) and (b), but for the checkerboard test carried out for the coseismic observation network including all of the available measurements (GPS, InSAR and LLC).

Figure S6. Synthetic and modelling residuals of the surface displacements for the checkerboard test shown in Fig. S5. In panels (a) and (b), the synthetic data are shown by black arrows for GPS data (or blue arrows for LLC in b) and residuals are shown by red colour. In panels (c) and (d), the modelling residuals for the synthetic InSAR data are colour-coded. The other symbols are the same as those in Fig. S4.

Figure S7. (a) Grid search results for λ^2 based on the cross-validation method, and (b) the surface displacement rates observed (black arrows) and modelling residuals (red arrows) of the interseismic backslip (Fig. 2a of the main text). The thick dashed line in panel (b) marks the location of the trench and the light dots indicate the fault plane used for interseismic modelling.

Figure S8. Grid search results for λ^2 based on 10-fold cross-validation for coseismic slip modelling (Mod_1) based on all available coseismic displacements.

Figure S9. Observations (black arrows for GPS data in panels (a) and (b), and blue arrows for LLC in panel b) and modelling residuals (red arrows in panels (a) and (b), coloured dots in panels (c) and (d) for InSAR data) of the coseismic slip of Mod_1 (Fig. 3 in the main text). The other symbols are identical to Fig. S4.

Figure S10. Grid search results for γ^2 based on 10-fold cross-validation ($\lambda^2 = 0.01$) for coseismic slip modelling (Mod_2).

Figure S11. Similar as Fig. S9, but for the Mod_2.

Figure S12. Modelling results using GPS, InSAR and LLC data for different model setups: (Mod_a) variable rake angle and the weight being 0.5/0.25/0.25 for GPS/InSAR/LLC, the same as Moreno *et al*. (2012); (Mod_b) rake $= 112^\circ$ and weight $= 0.5/0.25/0.25$; (Mod_c) variable rake angle and measurement uncertainties being included, instead of arbitrary weights as in Mod_a and Mod_b; (Mod_d) rake $= 112^\circ$ and the measurement uncertainties being considered.

Figure S13. Coseismic slip modelling results based on the continuous GPS measurements: (a) coseismic slip; (b) slip uncertainties. Observations (black arrows) and modelling residuals (red arrows) of the horizontal and vertical surface displacements are shown in panels (c) and (d). The star marks the hypocentre of the 2010 Maule earthquake. The symbols in panels (c) and (d) are the same as those in Fig. S4.

Figure S14. Modelling results taking the interseismic coupling of Moreno *et al*. (2010) as a constraint: (a) interseismic backslip rate calculated from Moreno's coupling model; (b) inverted coseismic slip model constrained by interseismic backslip in panel (a); (c) residual interseismic backslip rate after the Maule earthquake. (d) Mod_2 presented in the maintext for comparison. The star marks the hypocentre of the 2010 Maule earthquake.

Figure S15. Depth distribution of seismicity in the study region: the seismicity between 1970 and 2016 is extracted from the GCMT catalogue (Ekström *et al.* 2012 in the Supporting Information), the aftershocks of 2 yr after the 2010 Maule earthquake are from Rietbrock *et al.* (2012).

Please note: Oxford University Press is not responsible for the content or functionality of any supporting materials supplied by the authors. Any queries (other than missing material) should be directed to the corresponding author for the paper.